World Academy of Science, Engineering and Technology
International Journal of Mechanical and Mechatronics Engineering
Vol:11, No:10, 2017

Numerical Investigations on Dynamic Stall of a Pitching-Plunging Helicopter Blade Airfoil

Xie Kai, Laith K. Abbas, Chen Dongyang, Yang Fufeng, Rui Xiaoting

Open Science Index, Mechanical and Mechatronics Engineering Vol:11, No:10, 2017 publications.waset.org/10007951.pdf

***Abstract*—**Effect of plunging motion on the pitch oscillating NACA0012 airfoil is investigated using computational fluid dynamics (CFD). A simulation model based on overset grid technology and k - ω shear stress transport (SST) turbulence model is established, and the numerical simulation results are compared with available experimental data and other simulations. Two cases of phase angle φ = *0,* μ which represents the phase difference between the pitching and plunging motions of an airfoil are performed. Airfoil vortex generation, moving, and shedding are discussed in detail. Good agreements have been achieved with the available literature. The upward plunging motion made the equivalent angle of attack less than the actual one during pitching analysis. It is observed that the formation of the stall vortex is suppressed, resulting in a decrease in the lift coefficient and a delay of the stall angle. However, the downward plunging motion made the equivalent angle of attack higher the actual one.

***Keywords*—**Dynamic stall, pitching-plunging, computational fluid dynamics, helicopter blade rotor, airfoil.

I. Introduction

DYNAMIC stall is a term often used to describe the complex series of events that result in the dynamic delay of stall, on airfoils and wings experiencing unsteady motion, to angles significantly beyond the static-stall angle. This delay of stall, usually followed by large excursions in lift and pitching moment, has challenged aerodynamicists for many years [1]. Dynamic stall always occurs on helicopter rotor blades during forward flight mainly on retreating side (the retreating-blade condition; see Fig. 1 (a)) of the rotor disc [2]. The creation, movement and shedding of the dynamic stall vortex on helicopter rotor blades become more complex due to the blades not only pitch and plunge during forward flight. The rotor blades' pitching-plunging movement is illustrated in Fig. 1 (b). Although extensive recent experimental research studies [3], [4], numerical simulations [5]-[9], and combination of them [10] have been published, dynamic stall problems have not been addressed completely.

Over the last few decades, CFD has developed into a rich and diverse subject and is emerged as a major component of applied and basic fluid dynamic research along with theoretical and experimental studies. Simultaneous development of new computers, numerical algorithms, physical and chemical models of flow physics are responsible for the great impact of CFD in both basic and applied scientific/engineering problems. Presently, CFD methods are employed routinely for the estimation of various complex aerodynamic and propulsion flow parameters where experimental data cannot be obtained economically or feasibly. CFD has emerged as one of the important design tools along with the wind tunnels and other experimental testing and contributing significantly in reducing developmental cost and time for aerospace vehicle design.

In this paper, FLUENT software ver. 18, which represents a powerful tool of CFD, is used to investigate the interaction of plunging motion coupled with a pitch oscillating airfoil with the same oscillation frequency and high amplitude. A computational result is compared to available experimental data and simulated results in the literature. In general, a good result within engineering error margins is obtained. Discussions of the finding along with the pertinent conclusions are presented.

II. CFD Governing Equations

For any CFD problem, the general transport equation for property ϕ (general variable) is [11]

$$\underbrace{\partial(\rho\phi)/\partial t}_{\substack{\text{Rate of increase of}\\ \phi \text{ of fluid element}}} + \underbrace{\operatorname{div}(\rho\phi\mathbf{u})}_{\substack{\text{Net rate of flow of}\\ \phi \text{ out of fluid element}}} = \underbrace{\operatorname{div}(\Gamma \operatorname{grad}\phi)}_{\substack{\text{Rate of increase of}\\ \phi \text{ due to diffusion}}} + \underbrace{S_\phi}_{\substack{\text{Rate of increase of}\\ \phi \text{ due to sources}}} \quad (1)$$

where ρ is the density, t is the time, and $\mathbf{u}$ is the velocity vector. It clearly highlights the various transport processes: the rate of change term and the convective term on the left-hand side and the diffusive term (Γ =diffusion coefficient) and the source term respectively on the right-hand side. In order to bring out the common features we have, of course, had to hide the terms that are not shared between the equations in the source terms. Note that (1) can be made to work for the governing equations according to the symbols of each particular equation, i.e. continuity equation, momentum equations, and energy equation by setting $\phi = 1$, $\Gamma = S_\phi = 0$; $\phi = u_i$, $\Gamma = \mu$, $S_\phi = -\partial p/\partial x_i + S_M$; $\phi = T$, $\Gamma = k/C_\upsilon$, $S_\phi = -p \operatorname{div}\mathbf{u} + \Phi + S_i$, respectively. Φ is the dissipation function, $u_i \equiv (u_1 = u, u_2 = v, u_3 = w)$ is the velocity components in the direction $x_i \equiv (x_1 = x, x_2 = y, x_3 = z)$, C_v is

Xie Kai, MSc. candidate, Chen Dongyang, PhD candidate, Yang Fufeng, associate professor, and Rui Xiaoting, professor, at Institute of Launch Dynamics, Nanjing University of Science and Technology, Nanjing, 210094, People Republic of China (e-mail: xiekai1011@qq.com, 675886518@qq.com, fufengyang@aliyun.com, ruixt@163.net).

Laith K. Abbas is a professor at Institute of Launch Dynamics, Nanjing University of Science and Technology, Nanjing, 210094, People Republic of China (corresponding author, phone: 0086-25-84315901; fax: 0086-25-84315901; e-mail: laithabbass@yahoo.com).

The authors gratefully acknowledge the financial support of this research by Science Challenge Project (No.JCKY2016212A506-0104) and Natural Science Foundation of China Government (No. 11472135).

the specific heat, k is the Boltzmann constant relating temperature T and energy, p is the pressure, and S_M is the momentum source. Equation (1) is used as the starting point for computational procedures in the finite volume method by integrating the differential equation, and then to apply "Gauss divergence theorem", which for a vector **a** states $\int_{CV} \mathrm{div}(\mathbf{a}) = \int_{A} \mathbf{n}\cdot\mathbf{a}\,\mathrm{d}A$, leading to the following general conservation equation in integral form [12]

$$\underbrace{\partial/\partial t \int_{CV} \rho\phi \,\mathrm{d}V}_{\text{Rate of increase of } \phi} + \underbrace{\int_{A} \mathbf{n}\cdot(\rho\phi\mathbf{u})\,\mathrm{d}A}_{\text{Net rate of decrease of } \phi \text{ due to convection across boundaries}} = \underbrace{\int_{A} \mathbf{n}\cdot(\Gamma \mathrm{grad}\phi)\,\mathrm{d}A}_{\text{Net rate of increase of } \phi \text{ due to diffusion across boundaries}} + \underbrace{\int_{CV} S_\phi \,\mathrm{d}V}_{\text{Net rate of creation of } \phi} \tag{2}$$

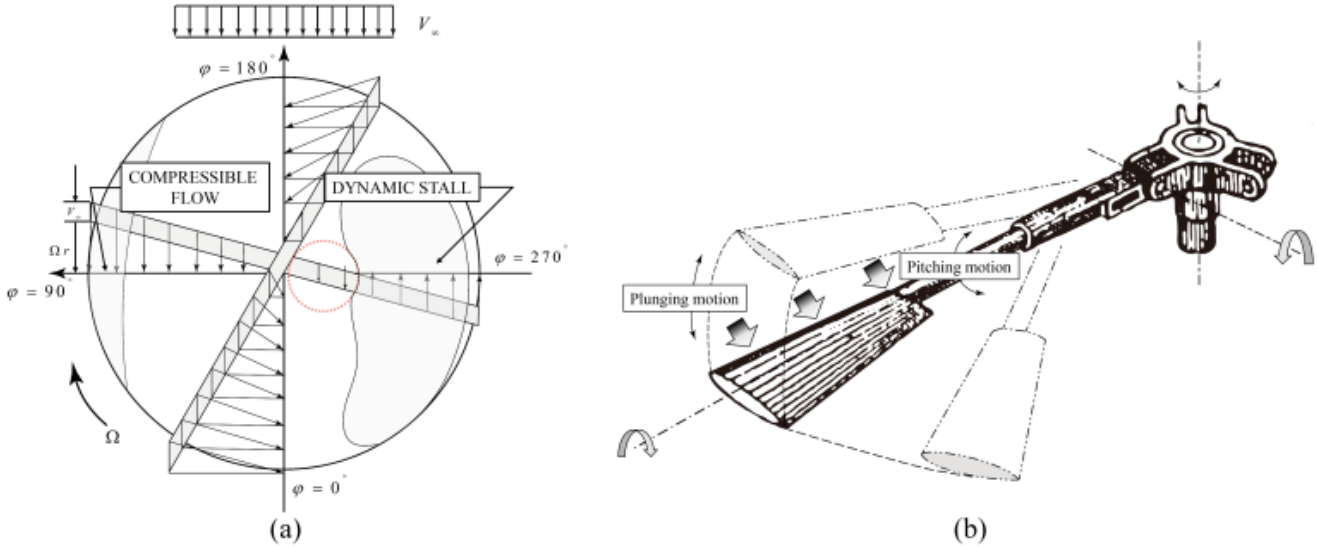

Fig. 1 (a) Sketch of rotor blades under work condition, and (b) Pitching-plunging motion

To calculate the flow pattern and scalar fields, (2) represents the conservation equations that need to solve using finite volume based CFD codes.

The treatment of turbulence in the Reynolds-Averaged Navier-Stokes (RANS) equations lies at the heart of most practical CFD approaches [12]. Decomposing the Navier-Stokes (NS) equations into the RANS equations makes it possible to simulate practical engineering flows, such as the airflow over aerospace vehicles. The Reynolds decomposition defines flow property f at this point as the sum of a steady mean component $\bar{f}$ and a time varying fluctuating component $f'(t)$ with zero mean value, i.e. $f = \bar{f} + f'(t)$. All other flow variables, i.e. all other velocity components, the pressure, temperature, density etc., will also exhibit this additional time-dependent behavior ($\mathbf{u} = \mathbf{U} + \mathbf{u}' \equiv u = U + u'$; $v = V + v'$; $w = W + w'$ and $p = P + p'$). Using averaging and substitution in (1), RANS equations end up with the following forms

$$\frac{\partial \rho}{\partial t} + \frac{\partial(\rho \bar{u}_i)}{\partial x_i} = 0,$$
$$\frac{\partial(\rho \bar{u}_i)}{\partial t} + \frac{\partial(\rho \bar{u}_i \bar{u}_j)}{\partial x_j} = -\frac{\partial \bar{p}}{\partial x_i} + \frac{\partial}{\partial x_j}\left[2\mu\left(S_{ij} - \frac{1}{3}S_{kk}\delta_{ij}\right)\right] + \frac{\partial}{\partial x_j}(-\rho \overline{u_i' u_j'}) \tag{3}$$

where $-\rho \overline{u_i' u_j'} = R_{ij}$; $S_{ij} = \frac{1}{2}\left(\frac{\partial \bar{u}_i}{\partial x_j} + \frac{\partial \bar{u}_j}{\partial x_i}\right)$ The viscosity, μ, is the property of the fluid and S_{ij} is the instantaneous strain rate tensor. Equation (3) then introduces a set of unknowns called the Reynolds stresses (R_{ij}) which are functions of the velocity fluctuations. There are several advantages of using RANS, such as less computational requirements than that required for the original NS equations. In addition, the mean flow velocity is calculated as a direct result without the need to average the instantaneous velocity over a series of time steps [12]. Therefore, the objective of the turbulence models for RANS equations is to compute R_{ij} to closure (3). This can be done by one of three main categories of RANS-based turbulence models, namely, linear eddy viscosity, nonlinear eddy viscosity and Reynolds stress. In the present research, SST $k-\omega$ turbulence model (integrates the advantages of $k-\varepsilon$ and $k-\omega$ models) developed by Menter [13], [14] is considered for R_{ij} computations. Boussinesq hypothesis is utilized in (3) to relate R_{ij} to the mean velocity gradients within the flow, i.e.

$$-\rho \overline{u_i' u_j'} = \mu_t\left(\frac{\partial \bar{u}_i}{\partial x_j} + \frac{\partial \bar{u}_j}{\partial x_i}\right) - \frac{2}{3}\left(\rho k + \mu_t \frac{\partial \bar{u}_k}{\partial x_k}\right)\delta_{ij} \tag{4}$$

Open Science Index, Mechanical and Mechatronics Engineering Vol:11, No:10, 2017 publications.waset.org/10007951.pdf

Open Science Index, Mechanical and Mechatronics Engineering Vol:11, No:10, 2017 publications.waset.org/10007951.pdf

where $\mu_t = \rho k/\omega$ is the turbulent (or eddy) viscosity, and k is the turbulent kinetic energy. For two-equation turbulence models such as the $k-\varepsilon$ and $k-\omega$ variants, the turbulent viscosity is computed through the solution of two additional transport equations for the turbulent kinetic energy and the specific dissipation rate, $\omega = \varepsilon/k$, where ε is the turbulence dissipation rate. Moreover, the SST $k-\omega$ is more accurate and reliable for a wider class of flows than the standard $k-\omega$, including adverse pressure gradient and separation flow. Menter's SST model is based on a mix of two equations $k-\varepsilon$ and $k-\omega$ turbulence models using a blending function F_1.

TABLE I
DETAILS OF SIMULATED CASES

Airfoil	NACA0012	
Pitching motion	$\alpha = \alpha_{mean} + \alpha_{amp}\sin(2\pi f\ t)$	
Reduced frequency	k	0.1
Mean angle	α_{mean}	10
Amplitude	α_{amp}	15
Plunging motion	$h = h_{amp}\sin(2\pi f\ t + \varphi)$	
Reduced frequency	k	0.1
Amplitude	h_{amp}	0.15
Phase difference	φ	$0, \pi$

III. CFD MODELING

A. Specification of Simulated Cases

In this study, a NACA0012 airfoil with pitch oscillating about a fixed axis at the 1/4 chord location has a reduced frequency $k = \omega c/2U_\infty$, where $\omega = 2\pi f$ and f is the oscillation frequency. The oscillating model is $\alpha = \alpha_{mean} + \alpha_{amp}\sin(2\pi f\ t)$. Here in, α_{mean} and α_{amp} are the mean angle of airfoil and the pitch oscillation amplitude, respectively. The plunge oscillating of airfoil NACA0012 can be written in the following form $h = h_{amp}\sin(2\pi f\ t + \varphi)$, where h_{amp} and φ are the plunge oscillation amplitude and the phase difference between the airfoil pitching and plunging oscillations, respectively. The details of the cases considered in this study are provided in Table I.

B. Grid Generation and Boundary Conditions

Simulations of the pitching and plunging motion of a NACA0012 airfoil are based on the dynamic overset grid technology. It is a newly developed grid technology which is created by a background grid (major grid) and a number of overset grids (minor grid) overlap the body, and the data are obtained by interpolating between main and overset grids. Here, the boundary conditions of a square domain with 40 times chord and O-grid layout with 30 times chord are defined as pressure-far-field with sea level condition and overset, respectively. These are generated by ICEM CFD (FLUENT 18.0). Meanwhile airfoil is no-slip wall condition. Around the airfoil, there are 340 nodes distributed with high resolution on the leading and trailing edges. The thickness of the cells around the airfoil is adapted for $y^+ \approx 1$ which utilized for the final grid mesh 49560 nodes and 49206 cells. Fig. 2 depicts a sketch of grid generation and boundary conditions.

C. Turbulence Model and Solver Set-Up

The solver used is steady-state density based solver. Energy equation is used for the simulation because the flow is compressible and also ideal gas equation is used. The two-equation SST $k-\omega$ turbulent model is chosen. A code written in C-Language is added to FLUENT platform as a user-defined function (UDF) to drive the motion of the pitching-plunging airfoil. The solution method is implicit formulation and Roe-FDS. The implicit formulation for time discretization is more stable and can be driven much harder to reach a converged solution in less time. The least square cell based gradient method is used. Second Order Upwind scheme for spatial discretization is used on convection and turbulent viscosity terms. The internal time step is determined by so called Courant number (CFL) which affects the solution speed and stability.

The CFL for the density-based implicit formulation is 5 [15]. It is often possible to increase the CFL, depending on the complexity of problem. However, it can be changed as the solution progresses. The input data then are set up for ambient condition (sea level) such as pressure and temperature (102.375 kPa, 304.8 K). The convergence criterion for the residuals is 1×10^{-5}. The computation is about 5 interactions/second using 16 cores for computations of a computer with 32 GB (RAM) and INTEL Xeon 32 cores. Total computation is performed less than 12 hours. The time step is 0.0001 s and it ran at least three loops (periods) of dynamic loads.

D. Validation

To verify the accuracy of the modeling and simulations, a pitching airfoil without plunging motion (Table I) is performed, and the results are compared with Lee's experiment [16] and Wang's numerical simulation [17]. The comparison of dynamic loads loops (periods) are plotted in Fig. 3 under the condition of Reynold number $R_e = 1\times10^5$. It reveals that the present results are closer to the experimental data at small angles of attack during upstroke than [15]. However, there are small oscillations during down-stroke which are small differences from experimental data. Probably the constants of SST $k-\omega$ model in the transport equation are based on simple flow condition in equilibrium. After flow separation, the flow experiences strong turbulence leading to difficulty in the prediction of aerodynamic loads after dynamic stall.

Open Science Index, Mechanical and Mechatronics Engineering Vol:11, No:10, 2017 publications.waset.org/10007951.pdf

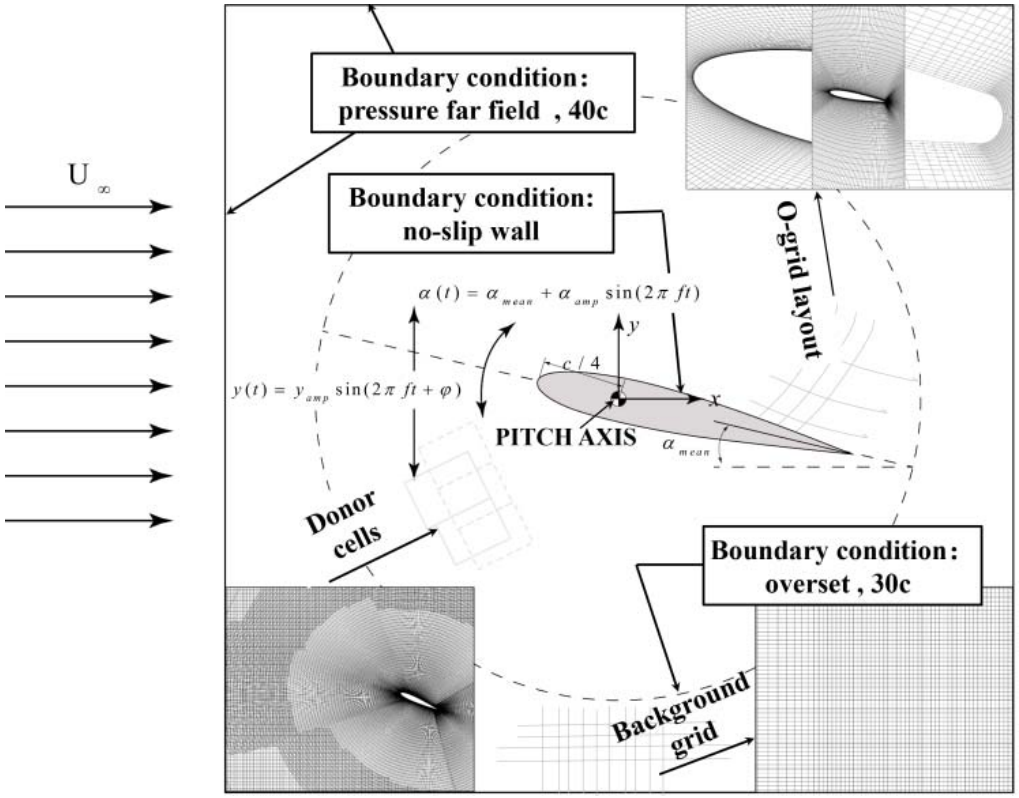

Fig. 2 Sketch of grid generation and boundary conditions

IV. Results and Discussion

In order to observe the effects of plunging motion, we simulated two cases of $\varphi = 0, \pi$ for $R_e = 1\times10^5$. All details are tabulated in Table I. Fig. 4 shows the displacement and velocity of plunging motion with the angle of attack variation. The red and blue lines represent $\varphi = 0$ and $\varphi = \pi$, respectively.

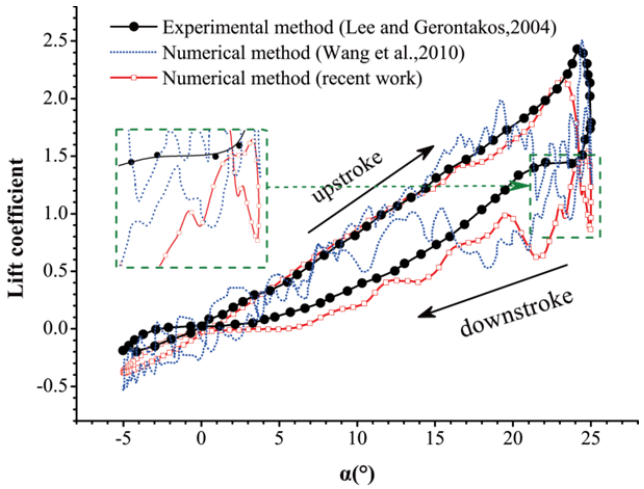

(a)

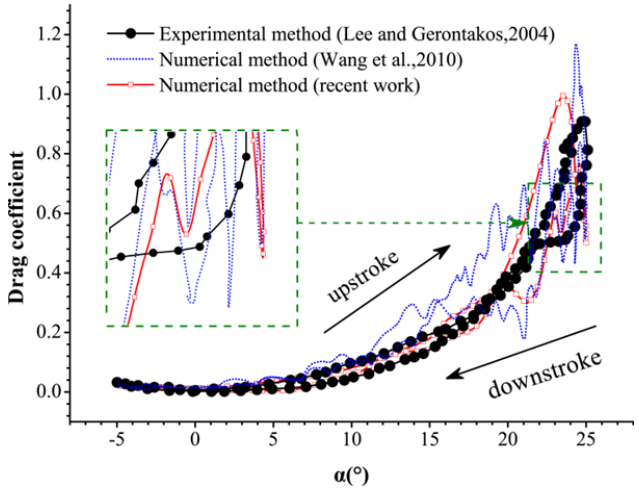

(b)

Fig. 3 Comparison of the dynamic loads loops with experimental data [16], numerical simulations [17] and the present work. (a) Lift coefficient, and (b) Drag coefficient

Open Science Index, Mechanical and Mechatronics Engineering Vol:11, No:10, 2017 publications.waset.org/10007951.pdf

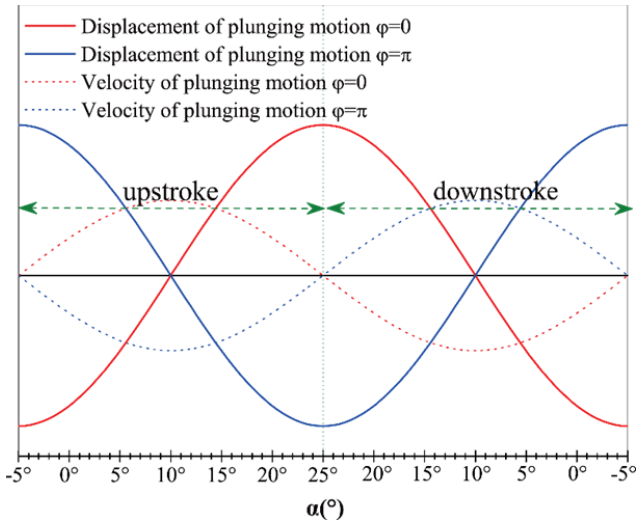

Fig. 4 Displacement and velocity of plunging motion

For $\varphi = 0$, the airfoil is accompanied with floating movement during upstroke (see Fig. 4 red curve). When $\alpha = 10^{\circ}$, the velocity of plunging motion reached the maximum value. As shown by the red line in Fig. 5 (a), the uplift movement suppressed the increase of the lift coefficient during upstroke, and the subsidence movement promoted the increase of the lift coefficient during downstroke, which caused the delay loop to be significantly reduced and the stall angle delayed about 1.76° . In the case where an airfoil is accompanied with subsidence movement during upstroke and uplift movement during downstroke (see Fig. 4 blue curve), the delay loop is enlarged and the stall angle advances about 8.83°. The drag coefficient of pitching-plunging motion is less than pure-pitching motion during upstroke, while it is more during downstroke as seen in Fig. 5 (b). Fig. 5 (c) reveals that the moment coefficient is closed with pure pitching. More details will be discussed in the following.

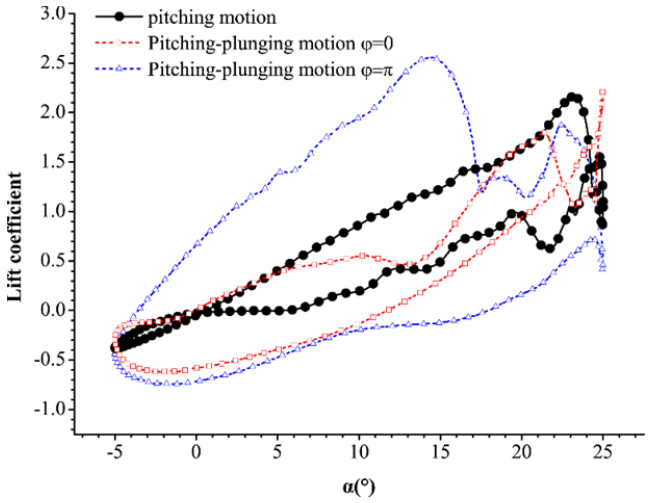

(a)

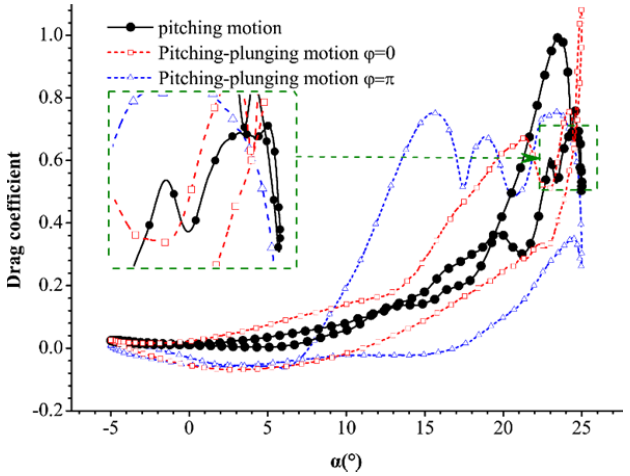

(b)

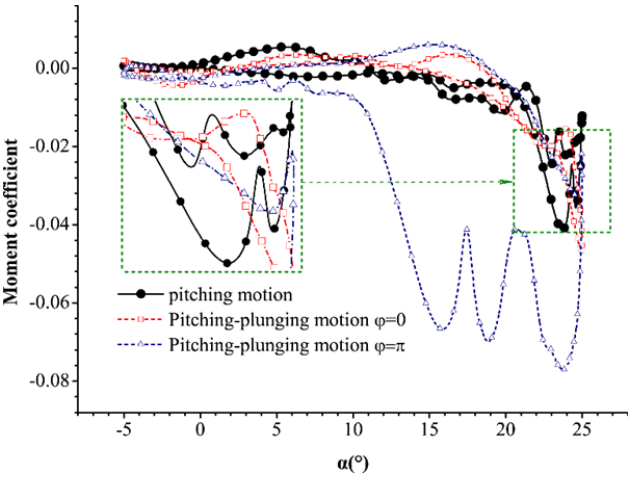

(c)

Fig. 5 The coefficients of lift (a), drag (b) and moment (c) of a pitching-plunging airfoil for $\varphi = 0, \pi$

For $\varphi = 0$, in the beginning, laminar flow is attached to the airfoil surface except in the small trailing edge region (Fig. 6 $\alpha = 4.98^{\circ} +$). Herein, the symbols '+' and '−' represent upstroke and downstroke, respectively. Then, the low pressure area on suction surface expanded and the low pressure area on pressure surface reduced, the lift coefficient began to be positive (Fig. 6 $\alpha = 12.35^{\circ} +$). At the same time, the slope of the lift coefficient increased gradually due to the weakening of the floating motion. The reverse flow moved from tailing edge to leading edge while the tailing edge vortex appeared at $\alpha = 23.89^{\circ} +$. The leading edge vortex is formed which leads to a significant increase in the slope of the lift coefficient at $\alpha = 24.36^{\circ} +$. The leading vortex continued to expand to cover the entire airfoil meanwhile the lift coefficient reached the peak at $\alpha = 24.99^{\circ} +$. The secondary vortex is expanded and the main vortex separated from the airfoil surface at $\alpha = 24.77^{\circ} -$ which caused a rapid decline in lift coefficient. Then, the leading edge vortex and the secondary vortex are expanded and the tailing edge vortex rapidly became large and weaker from

tailing edge. The lift coefficient reached the peak of downstroke at $\alpha = 24.13^{\circ}+$. Then, the lift coefficient declined gradually with the main vortex generation, moving and separation. Lift coefficient is slightly improved due to the promotion of sinking movement at $\alpha = 9.94^{\circ}+$.

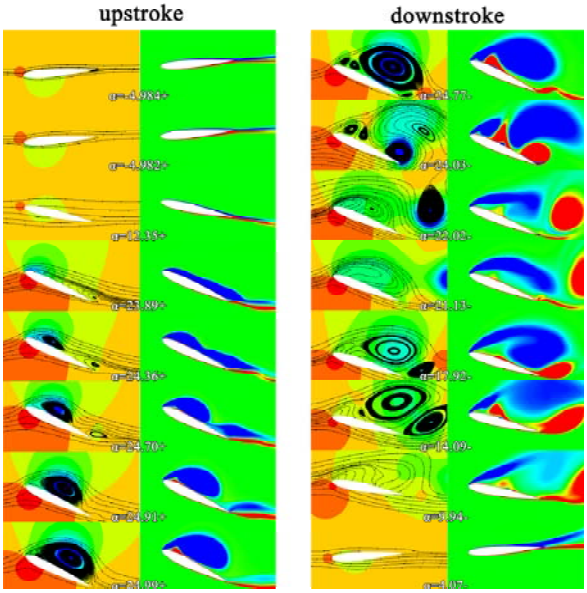

Fig. 6 Pressure superimposed with flow streamlines and dimensionless vorticity magnitude for $\varphi = 0$

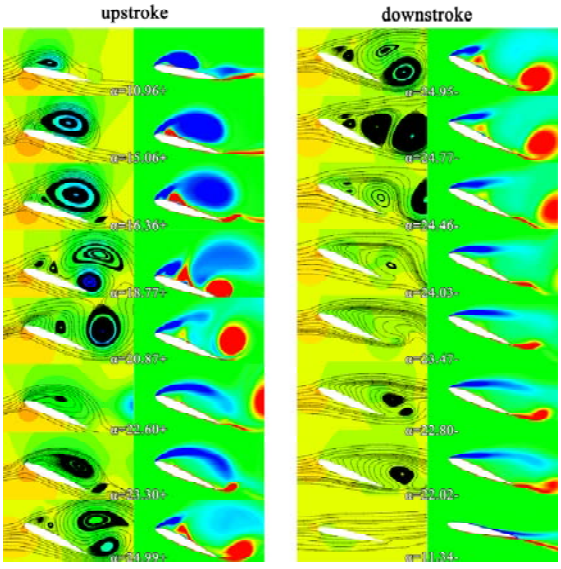

Fig. 7 Pressure superimposed with flow streamlines and dimensionless vorticity magnitude for $\varphi = \pi$

For $\varphi = \pi$ (Fig. 7), the lift coefficient slope significantly increased due to the formation of the leading edge vortex at $\alpha = 10.96^{\circ}+$. The leading edge vortex continued to expand to cover the entire chord while the lift coefficient reached the peak at $\alpha = 15.06^{\circ}+$. The stall is generated because of vortex separation. After the main vortex shedding, the trailing edge vortex increased rapidly, while the small leading edge vortex and the secondary vortex moved to the trailing edge and covered the airfoil again. The lift coefficient reached the secondary peak at $\alpha = 22.60^{\circ}+$. The vortex is shed and turned to attached flow during downstroke.

V. Conclusion

The simulation model based on overset grid and the SST $k-\omega$ turbulence model is carried out to simulate the flow around of a dynamic stall of NACA0012 airfoil. The simulation results are in good agreement with the experimental data. However, the results after stall should be improved. For a pitching airfoil, the upward plunging motion made the equivalent angle of attack less than the actual one. It suppressed the formation of the stall vortex, resulting in a decrease in the lift coefficient, a delay of the stall angle and a reduction in the delay loop. In contrast, the downward plunging motion made the equivalent angle of attack higher than the actual one.

References

[1] L. W. Carr, "Progress in analysis and prediction of dynamic stall," *Journal of Aircraft*, vol. 25(1), pp. 6-17, 2012.
[2] W. Geissler, M. Raffel, G. Dietz, et al. "Helicopter aerodynamics with emphasis placed on dynamic stall," in *EUROMECH Colloquium 464b Wind Energy*, DLR, 2007.
[3] T. Lee and S. Basu, "Measurement of unsteady boundary layer developed on an oscillating airfoil using multiple hot-film sensors," *Experiments in Fluids*, Vol. 25(2), pp. 108–117, 1998.
[4] H. Sadeghi, and M. Mani, "Measurements of the flow field behind a helicopter blade using the hot-wire anemometry," *Journal of Information Communication Technology*, Vol. 2, pp. 32–39, 2009.
[5] W. J. McCroskey, "The phenomenon of dynamic stall," NASA Technical report TM-81624, 1981.
[6] W. J. McCroskey, "Unsteady airfoils," *Annual Review of Fluid Mechanics*, Vol. 14(1), pp. 285-311, 2003.
[7] G. Barakos and D. Drikakis, "Computational study of unsteady turbulent flows around oscillating and ramping airfoil," *International Journal of Numerical Methods in Fluids*, Vol. 42(2), pp. 163–186, 2003.
[8] W. Sheng, R. A. Galbraith, and F. N. Coton, "A modified dynamic stall model for low Mach numbers," *ASME Journal of Solar Energy Engineering*, Vol. 130(3), pp. 310–313, 2008.
[9] K. Gharali and D. A. Johnson, "Numerical modeling of an S809 airfoil under dynamic stall, erosion and high reduced frequencies," *Applied Energy*, Vol. 93 (5), pp. 45-52, 2012.
[10] P. Wernert, W. Geissler, M. Raffel and J. Kompenhans, "Experimental and numerical investigations of dynamic stall on a pitching airfoil," *AIAA Journal*, Vol. 34 (5), pp. 982–989, 1996.
[11] E. D. V. Bigarella, J. L. F. Azevedo and O. A. F. Mello, "Normal force calculations for rocket-like configurations," *Journal of the Brazilian Society of Mechanical Science and Engineering*, Vol. 26 (3), pp. 290-296, 2004.
[12] Reynolds-Averaged Navier-Stokes Equations, article, 2009, http://www.symscape.com/reynolds-averaged-navier-stokes-equations Accessed on 05/06/2017.
[13] F. R. Menter, "Zonal two equation k-ω turbulence models for aerodynamic flows," AIAA-93-2906, 1993.
[14] F. R. Menter, "Two-equation eddy-viscosity models for engineering applications," *AIAA Journal*, Vol. 32(8), pp. 1598-1605, 1994.
[15] S. S. Benadict Bensiger and N. Prasanth, "Analysis of bi-convex aerofoil using CFD software at supersonic and hypersonic speed," *Elixir Mechanical Engineering*, Vol. 53, pp. 11695-11698, 2012.
[16] T. Lee and P. Gerontakos, "Investigation of flow over an oscillating airfoil," *Journal of Fluid Mechanics*, Vol. 512, pp. 313-341, 2004.
[17] S. Wang, S., D. B. Ingham, L. Ma, et al., "Numerical investigations on dynamic stall of low Reynolds number flow around oscillating airfoils," *Computers and Fluids*, Vol. 39(9), pp. 1529-1541, 2010.

Open Science Index, Mechanical and Mechatronics Engineering Vol:11, No:10, 2017 publications.waset.org/10007951.pdf